



# 1 Mitigating Radome Induced Bias in X-Band Weather Radar 2 Polarimetric moments using Adaptive DFT Algorithm.

3 Thiruvengadam PADMANABHAN<sup>1,2</sup>, Guillaume LESAGE<sup>1</sup>, Ambinintsoa Volatiana  
4 RAMANAMAHEFA<sup>1</sup>, and Joël VAN BAELEN<sup>1</sup>

5

6 <sup>1</sup>LACY, Université de La Réunion/CNRS/MétéoFrance, Saint-Denis, La Réunion.

7 <sup>2</sup>School of Meteorology, University of Oklahoma, Norman, Oklahoma, USA.

8

9 Correspondence to: Thiruvengadam PADMANABHAN (thiruvengadam7892@gmail.com) and Joël VAN BAELEN ([joel.van-](mailto:joel.van-baelen@univ-reunion.fr)  
10 [baelen@univ-reunion.fr](mailto:joel.van-baelen@univ-reunion.fr))

11

12 **Abstract.** In recent years, the application of compact and cost-effective deployable X-band polarimetric radars has gained in  
13 popularity, particularly in regions with complex terrain. The deployable radars generally use a radome constructed by joining  
14 multiple panels using metallic threads to facilitate easy transportation. As a part of the ESPOIRS project, Laboratoire de  
15 l'Atmosphère et des Cyclones has acquired an X-band meteorological radar with four panel radome configuration. In this study,  
16 we investigated the effect of the radome on the measured polarimetric variables, particularly differential reflectivity and differential  
17 phase. Our observations reveal that the metallic threads connecting the radome panels introduce power loss at vertical polarization,  
18 leading to a positive bias in the differential reflectivity values. To address the spatial variability bias observed in differential  
19 reflectivity and differential phase, we have developed a novel algorithm based on the Discrete Fourier Transform. The algorithm's  
20 performance was tested during an intense heavy rainfall event caused by the Batsirai cyclone on Reunion Island. The comparative  
21 and joint histogram analysis demonstrates the algorithm's effectiveness in correcting the spatial bias in the polarimetric variables.

22 **Keywords:** Radome joints, Spatial bias, X-band Weather radar, ZDR, PHIDP, Adaptive DFT algorithm, Polarimetric variables,  
23 Batsirai cyclone, Multi-panel radome.

24

## 25 1. INTRODUCTION

26 Doppler weather radars provide comprehensive precipitation measurements at high spatial resolution, offering valuable insights  
27 into the orography-influenced precipitation processes (Georgis et al., 2000). Among different frequency bands, X-band radars have  
28 gained popularity due to their compact size and affordable cost, making them well-suited for deployment in areas with challenging  
29 topography. Additionally, modern polarimetric technology has dramatically enhanced the ability of X-band radars to estimate  
30 precipitation, overcoming their traditional limitation of high attenuation rates in the rain (Ryzhkov et al., 1994). The ESPOIRS  
31 (Etude des Systèmes Précipitants de l'Océan Indien par Radars et Satellites) project implemented by LACy (Laboratoire de  
32 l'Atmosphère et des Cyclones) has utilized the advantages of X-band polarimetric radar to examine the dynamics and variability  
33 of intense tropical precipitation at the local scale, particularly its interaction with the relief of the island. Initially, an X-band radar  
34 operating at 9.41 GHz was deployed south of Reunion Island (Figure 1a) to investigate heavy rainfall and the pronounced relief  
35 effects that may contribute to rainfall intensification. Later, the radar was installed in Seychelles and Madagascar to explore  
36 different geographical and meteorological contexts.



37 Although X-band polarimetric radar offers advantages over single polarization radars, maintaining the accuracy of its polarimetric  
38 data requires rigorous quality control (Park et al., 2005). One factor that can impact the performance of the radars is the radome.  
39 While they play a protective role, radome can passively affect the observations due to material-related transmission losses and  
40 variations in sidelobe levels (Figueras i Ventura et al., 2021; Mishra et al., 2014). Mainly, radome panels with metallic threads at  
41 their joints, common in mobile radars, can introduce biases in polarimetric observations (Figueras i Ventura et al., 2021; Gourley  
42 et al., 2006). The ESPOIRS X-band radar is protected by a composite radome with a 1.435m base diameter and 2m height,  
43 consisting of four fiberglass-reinforced lateral segments attached through horizontally aligned metal nuts and bolts arranged along  
44 the vertical axis (Figure 1b, 1c). Radar data from the Batsirai cyclone on 3 February 2022 show significant biases in differential  
45 reflectivity (ZDR) and differential phase (PHIDP). One of the objective of this study is to identify the source of these biases and  
46 hypothesize that they originate from the radome metal joints.

47 In similar scenarios, efforts have been made to address biases using spatial calibration curves from radar data (Figueras i Ventura  
48 et al., 2021; Gourley et al., 2006). However, the stochastic nature of radar measurements introduces inherent uncertainty into  
49 calibration curves, leading to an overall increase in measurement uncertainty. Previous investigations have also recommended the  
50 implementation of a seamless monoblock radome to mitigate spatial bias, as it eliminates the presence of joints and, subsequently,  
51 any bias. Nevertheless, the unique design of the portable ESPOIRS X-band radar, which prioritizes ease of transportation, presents  
52 inherent challenges in adopting a monoblock radome solution. To address this challenge, this study proposes an adaptive Discrete  
53 Fourier Transform (DFT) based algorithm to mitigate the bias. This algorithm effectively utilizes the information available in radar  
54 scans and enables the correction of the ZDR and PHIDP moments for various scan strategies.

55 The distinguishing feature of this algorithm is its capacity for dynamic threshold adjustment in the correction of frequency values  
56 generated by the DFT based on the characteristics of radar moments. Such adaptivity sets this algorithm apart from traditional  
57 methods (Figueras i Ventura et al., 2021; Gourley et al., 2006), which employ fixed spatial calibration curves. To assess the  
58 performance of the proposed algorithm, it is applied to correct the ZDR and PHIDP radar scans obtained during an intense heavy  
59 rainfall event caused by the passage of the Batsirai cyclone in the vicinity of Reunion Island on February 2 to 4, 2022. Section II  
60 focuses on the source of the spatial bias in ZDR, offering insights into the factor responsible for this bias. The adaptive DFT  
61 algorithm proposed in this study is introduced in section III, providing a discussion of its mathematical formulation. Section IV  
62 assesses the proposed algorithm's performance through comparative and joint histogram analysis. Section V summarizes the key  
63 points of the study and outlines the direction of future research to test further and enhance the algorithm's performance.

## 64 2. SOURCE OF BIAS

65 To elucidate the origins of positive bias in PHIDP measurements and ascertain its underlying causes, this study employs a  
66 comprehensive approach involving the calculation of PHIDP offsets for all PPI scans conducted on the 2/3/2022 case study,  
67 following the technique outlined in previous works (Figueras i Ventura et al., 2012), which utilized PHIDP offsets to discern the  
68 influence of radome joints. The findings in Figure 1d exhibit a box plot distribution of PHIDP offsets across various azimuth  
69 angles. Figure 1d shows a sinusoidal azimuthal pattern with four periods in the PHIDP offset. Strikingly, a distinct correlation  
70 emerges between the azimuthal period positions of the PHIDP offsets and the orientation of the radome joints, with notable  
71 alignment occurring at approximately 355, 85, 175 and 265 degrees. This observation strongly suggests that the metallic threads  
72 and joint configuration are the key factors contributing to the bias in PHIDP. The localization of the bias near the joints is due to  
73 signal phase sensitivity to path length and material properties. Radome metal joints can introduce significant phase shifts in specific



74 polarizations, impacting PHIDP measurements when signal paths intersect with these joints (Li et al., 2017), explaining the  
75 observed PHIDP offset collocation with the radome joint direction.

76 The positive bias observed in ZDR (Figure 2a) can result from either an increase in horizontal reflectivity values (ZH) or a decrease  
77 in vertical reflectivity values (ZV). To ascertain the cause of the positive bias in ZDR, the temporal median of horizontal and  
78 vertical reflectivity obtained from RHI scan angles of 28, 300, 45 and 76 degrees on 3rd February 2022 were computed.  
79 Subsequently, for each median RHI scan at 28, 300, 45 and 76 degrees of azimuth respectively, elevation angles exhibiting positive  
80 ZDR bias (70, 70, 36, and 34) and unbiased elevation angles (66, 67, 31, and 27) were identified for both horizontal and vertical  
81 polarization and compared as shown in Figure 2a-2d. The biased (red, blue) and unbiased (black, green) elevation angles were  
82 chosen sufficiently close to each other to ensure that the same hydrometeor characteristics were observed.

83 Figures 2a and 2b show that the horizontal reflectivity values in biased and unbiased elevation angles (red, black) exhibit a  
84 consistent covariation pattern with a negligible offset. Consequently, one would expect the vertical reflectivity values (blue, green)  
85 to follow a similar trend. However, it is observed that the vertical reflectivity values correlate with each other but with an offset.  
86 Specifically, the biased elevation angle's vertical reflectivity (blue) has a negative offset compared to the unbiased elevation angle's  
87 vertical reflectivity (green). At lower elevation angles of RHI scans, where the variance of reflectivity values across the range  
88 direction is limited, a noticeable decrease in vertical reflectivity in the biased region is prominent. Specifically, at lower elevation  
89 angles of the RHI scans at 45 and 76 degrees of azimuth (Figure 2c and 2d), the vertical reflectivity values in the biased region are  
90 noticeably lower than their corresponding horizontal and vertical reflectivity values in the unbiased region. This indicates that the  
91 metal joints have exerted a notable influence on the propagation of microwaves, particularly regarding vertical polarization. This  
92 influence has led to a systematic bias in ZDR.

93 From Figures 4a and 4c, it can be noted that PHIDP and ZDR exhibit biases at somewhat different azimuth angle locations. The  
94 observed bias in ZDR at varying angles, compared to the bias in PHIDP, can be attributed to distinct scattering characteristics. The  
95 ZDR's azimuthal bias could arise from factors related to the scattering of incident power from the main lobe around the metallic  
96 threads, which could potentially amplify the impact of the side lobes. These increased side lobe levels cause more energy to be  
97 radiated or received in undesirable directions, potentially amplifying susceptibility to noise or interference from those directions  
98 (Frech et al., 2013). This differs from PHIDP's bias, which is primarily influenced by the path length the radar signals traverse (Li  
99 et al., 2017). Hence, the PHIDP bias are observed in the direction of the radome joints. Detailed simulations or measurements are  
100 imperative for a comprehensive understanding of the precise impact of radome joints on side lobe levels, phase delays, and their  
101 correlation with ZDR and PHIDP.

### 102 3. ADAPTIVE DFT ALGORITHM

103 This study introduces a DFT algorithm to mitigate the spatial bias present in the polarimetric variables. The correction procedure  
104 starts by performing a Discrete Fourier transform on a single radar scan, which, in this case, corresponds to the 76° azimuth RHI  
105 scan measured on 02/03/2022 01:08 UTC (Figure 3a). A one-dimensional DFT is applied along the range direction to process the  
106 polarimetric variable  $x$  for a particular azimuth or elevation angle  $\theta$  and  $N$  total range gates, as shown in equation 1, where  $n$  and  
107  $k$  represent the range gate and frequency index, respectively. The transformation  $F[k]$  is repeated for each angle  $\theta$ , respectively  
108 azimuth for PPI scans and elevation for RHI scans, systematically covering the entire radar scan to obtain  $F[\theta, k]$ .



109 Subsequently, the power spectrum ( $P[\theta, k]$ ) is calculated from the obtained Fourier transform ( $F[\theta, k]$ ) for each azimuth/elevation  
 110 angle, as depicted in Figure 3c. In Figure 3c, a three-dimensional representation is shown, illustrating the power spectrum obtained  
 111 from the DFT for each elevation angle of the RHI scan. Notably, the power value of the zero frequency component ( $P[\theta, 0]$ ) derived  
 112 from various elevation angles, representing the DFT's DC component, reveals three distinct peaks corresponding to the spatial bias  
 113 pattern observed in Figure 3a's RHI scan. This indicates that a bias caused by the radome joints will result in a constant positive  
 114 increase of the magnitude all along the range, an offset, which will show up as an increase in the power value of the DC component  
 115 of the DFT spectrum.

116

$$117 \quad F[\theta, k] = \sum_{n=0}^{N-1} e^{-2\pi j \frac{kn}{N}} x[\theta, n] \quad \text{for } 0 \leq k < N \quad (1)$$

118

119 To address this bias, a correction factor ( $A/B$ ) is introduced to filter the three peaks (Figure 3d) associated with the spatial bias.  
 120 Notably, the correction factor is only applied to the DC component values ( $F[\theta, 0]$ ) that exceed a certain adaptive threshold.

121

$$122 \quad F[\theta, 0]' = \begin{cases} F[\theta, 0] \times \frac{A}{B} & \text{if } P[\theta, 0] > \text{Median}(P[\theta, 0]) \\ F[\theta, 0] & \text{otherwise} \end{cases} \quad (2)$$

123

124 The threshold value is determined based on the moving median window of the power spectrum at the zeroth frequency  
 125 ( $\text{Median}(P[\theta, 0])$ ). The correction factor is calculated as the ratio between the median values of  $F[\theta, 0]$  corresponding to the  
 126 power values below the threshold (A) and the median values of  $F[\theta, 0]$  corresponding to the power values above the threshold  
 127 (B).

128

$$129 \quad A = \text{Median}(F[\theta, 0]) | P[\theta, 0] < \text{Median}(P[\theta, 0]) \quad (3)$$

$$130 \quad B = \text{Median}(F[\theta, 0]) | P[\theta, 0] > \text{Median}(P[\theta, 0]) \quad (4)$$

$$131 \quad P[\theta, 0] = \sqrt{\text{Real}(F[\theta, 0])^2 + \text{Img}(F[\theta, 0])^2}^2 \quad (5)$$

132 Consequently, the zeroth frequency values that surpass the threshold are multiplied by the calculated correction factor, while the  
 133 remaining values are left uncorrected. Figure 3d shows the power  $P[\theta, 0]$  from the DC component is characterized by distinct peaks  
 134 alongside the depiction of the adaptive threshold values and the reduced power after applying the correction factor. To derive the  
 135 corrected ZDR image (Figure 3b), an inverse Fourier transform is performed on all frequencies, encompassing the corrected DC  
 136 component.

137

$$138 \quad x[\theta, n] = \frac{1}{N} \sum_{k=0}^{N-1} e^{-2\pi j \frac{kn}{N}} F[\theta, k] \quad (6)$$

139

#### 140 4. ASSESSMENT OF ADAPTIVE DFT FILTERING ALGORITHM EFFICIENCY

141 The performance of the adaptive DFT filtering algorithm is assessed across different scan strategies (PPI and RHI) and different  
 142 polarimetric moments (ZDR and PHIDP) to determine its effectiveness. Figures 3a and 4a show increased spatial variability of  
 143 ZDR at specific azimuth and elevation angles of RHI and PPI scans, respectively, with a maximum variability of around 1.5-2 dB  
 144 observed. Similarly, Figures 4c and 5a depict increased spatial variability of PHIDP in PPI and RHI scans, with a magnitude of



145 variability around 8 to 10 degrees. The application of the algorithm led to a substantial reduction in variability, as shown in Figures  
146 3b, 4b, 4d and 5b. The proposed algorithm reduced the spurious ZDR variability from 1.5-2 dB to 1-1.34 dB, and the PHIDP  
147 variability was reduced to less than 5 degrees. The results indicate the algorithm's effectiveness in mitigating spatial variability in  
148 both ZDR and PHIDP values across all elevation angles and scanning strategies.

149 The relationship between ZDR and ZH provides insights into how raindrops deviate from a perfect spherical shape. Larger  
150 raindrops exhibit higher horizontal reflectivity and have their long axis oriented in the horizontal direction compared to the vertical  
151 direction, thereby showing signatures of higher ZDR values. Conversely, for lower values of horizontal reflectivity (less than 30  
152 dBZ), we generally expect a ZDR value of nearly zero dB due to the near spherical shape of small drops. Therefore, comparing  
153 the relationship between ZH and ZDR before and after applying the algorithm (Figure 6) shows how the correction has brought  
154 the biased ZDR close to the expected value. Figures 6a and 6b show the joint histogram of ZDR and ZH for all the PPI scans  
155 conducted on 3 February 2022 before and after applying the correction algorithm, with the marginal distribution of ZH in the top  
156 and the marginal distribution of ZDR on the right side. Likewise, figures 6c and 6d show the joint histogram of ZDR and ZH for  
157 all the RHI scans on the same date, before and after applying the correction algorithm. As these figures capture the data before any  
158 attenuation correction, the reflectivity distribution ranges from light drizzle (near zero dBZ) to heavy rainfall ( $\approx 40$  dBZ). It can be  
159 observed from Figure 6a, 6c that the distribution of ZDR extends significantly beyond 2dB for reflectivity values below 30 dBZ.  
160 Such increases arise from the spatial positive bias in ZDR discussed in view of Figures 3a and 4a. The impact of the developed  
161 algorithm on the distribution of ZDR is highlighted in Figures 6b and 6d. Following the correction, the mean distribution of ZDR  
162 shifts towards values closer to zero, approaching the theoretical values at lower reflectivity. Furthermore, the correction also results  
163 in a noticeable increase in negative values of ZDR, indicating the presence of differential attenuation fingerprints, a common  
164 occurrence in X-band radar systems, which were not as discernible before the correction. Figures 6b and 6d reveal the impact of  
165 the algorithm in successfully addressing the positive bias in ZDR.

## 166 5. CONCLUSION

167 This study investigates the impact of radome joints on the polarimetric variables of a portable X-band weather radar. The radome  
168 design introduces spatially dependent biases in polarimetric variables due to preferential loss of power in vertical polarization  
169 caused by metallic thread alignment. Due to the stochastic nature of radar measurements, these spatial errors exhibit variability  
170 across different scans. This study proposes a novel adaptive DFT algorithm to address the changing bias. The algorithm is  
171 formulated with the understanding that the bias caused by the radome joints remains constant along the range. Consequently, the  
172 DFT applied along the range exhibits an increase in magnitude in the zeroth frequency component (DC) for azimuth angles aligned  
173 with the radome joint positions compared to those misaligned. This leads to varying offset values of polarimetric variables across  
174 azimuths and elevations depending on the radar beam position with respect to radome joint positions. The algorithm detects and  
175 reduces the spatial bias pattern by suppressing the increase in offset values.

176 The algorithm's performance in mitigating the positive spatial bias in ZDR and PHIDP is evaluated by applying the algorithm in  
177 the PPI and RHI polarimetric variable scans measured during the Batsirai cyclone event on 3 February 2022. The results show that  
178 the adaptive DFT algorithm presented herein effectively addresses the spatial biases, enhancing the accuracy of ZDR and PHIDP  
179 measurements regardless of the scan type.

180 As the primary source of spatial bias originates from vertical polarization, the algorithm's effectiveness is further validated by  
181 examining the relationship between ZH and ZDR values. Notably, the correction reduces the positive bias observed in ZDR at



182 lower reflectivity levels, bringing the mean ZDR value closer to the expected levels. Additionally, the algorithm reveals negative  
183 ZDR values, indicating the presence of attenuation fingerprints.

184 The proposed algorithm has limitations related to sample size and precipitation type. To effectively distinguish between  
185 meteorological targets and bias, it requires a large, noise-free sample along the range direction. Additionally, its performance relies  
186 on suppressing variations in the magnitude of the DC component of DFT observed across continuous azimuth angles. As a result,  
187 the algorithm performs optimally in scenarios characterized by uniform precipitation, such as stratiform precipitation and large  
188 convective systems that cover extensive areas around the radar. However, for isolated or scattered precipitation systems located in  
189 limited range and azimuth gates, the algorithm's performance needs to improve due to its inability to capture variations in the DC  
190 component magnitude derived from the DFT. To advance future research and potential improvements, an area of interest lies in  
191 evaluating the proposed algorithm's performance by conducting measurements both with and without the radome. An additional  
192 consideration is the possibility of incorporating a seamless monoblock radome as a future plan.

193

#### 194 **Data availability**

195 All radar data is available at [https://geosur.osureunion.fr/thredds/catalog/researchprogram/espoirs/1-](https://geosur.osureunion.fr/thredds/catalog/researchprogram/espoirs/1-Saint_Joseph/RADAR/Data/az-vol-75-0125-1to25deg-2022-01/2022/02/catalog.html)  
196 [Saint\\_Joseph/RADAR/Data/az-vol-75-0125-1to25deg-2022-01/2022/02/catalog.html](https://geosur.osureunion.fr/thredds/catalog/researchprogram/espoirs/1-Saint_Joseph/RADAR/Data/az-vol-75-0125-1to25deg-2022-01/2022/02/catalog.html). For information on rain gauge data, please  
197 send requests to [ambinintsoa.ramanamahefa@univ-reunion.fr](mailto:ambinintsoa.ramanamahefa@univ-reunion.fr) or visit the Météo France website [https://portail-](https://portail-api.meteofrance.fr/web/fr/api/DonneesPubliquesObservation)  
198 [api.meteofrance.fr/web/fr/api/DonneesPubliquesObservation](https://portail-api.meteofrance.fr/web/fr/api/DonneesPubliquesObservation)

#### 199 **Code availability**

200 The code is available upon request from the authors

#### 201 **Author Contributions**

202 Thiruvengadam PADMANABHAN developed the algorithm, implemented the data analysis and wrote the paper, Guillaume  
203 LESAGE and Ambinintsoa Volatiana RAMANAMAHEFA contributed to the implementation of the methodology and revised the  
204 paper, Joël VAN BAELEN revised the paper and led the ESPOIRS project and radar field deployments.

#### 205 **Competing interests**

206 The authors declare that they have no conflict of interest.

#### 207 **Acknowledgment**

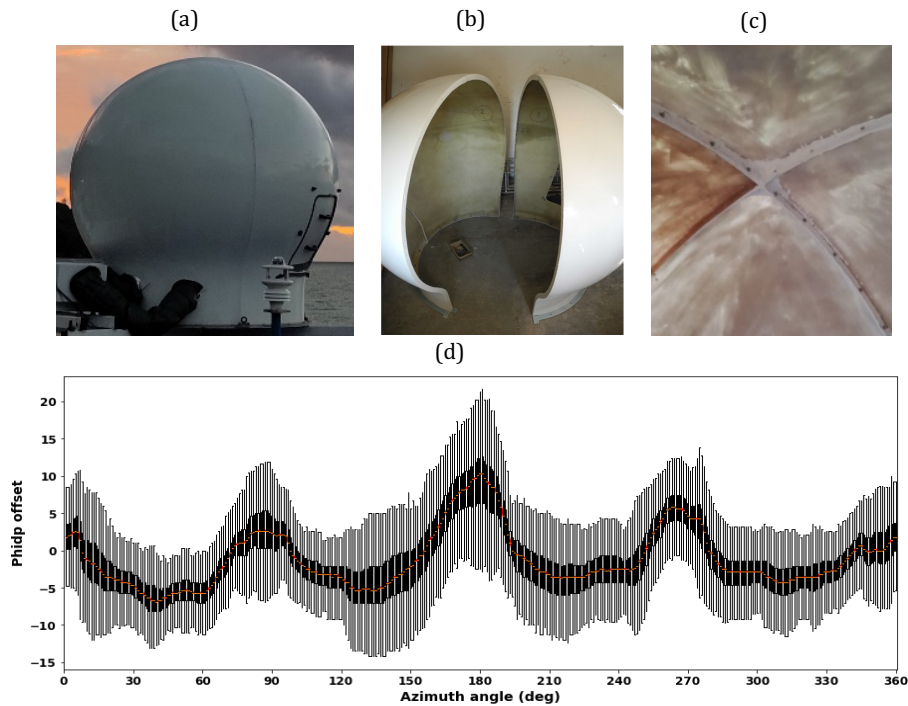
208 This work is part of the INTERREG V ESPOIRS project (Study of Precipitating Systems in the Indian Ocean by Radar and  
209 Satellites). The ESPOIRS scientific program is led by LACy (University of La Réunion / CNRS / MétéoFrance) and funded by the  
210 European Union (FEDER program - GURDTI/20201589-0021087), the Réunion Region, SGAR-Réunion, the French State (CPER) and the University of La Réunion.

212

213

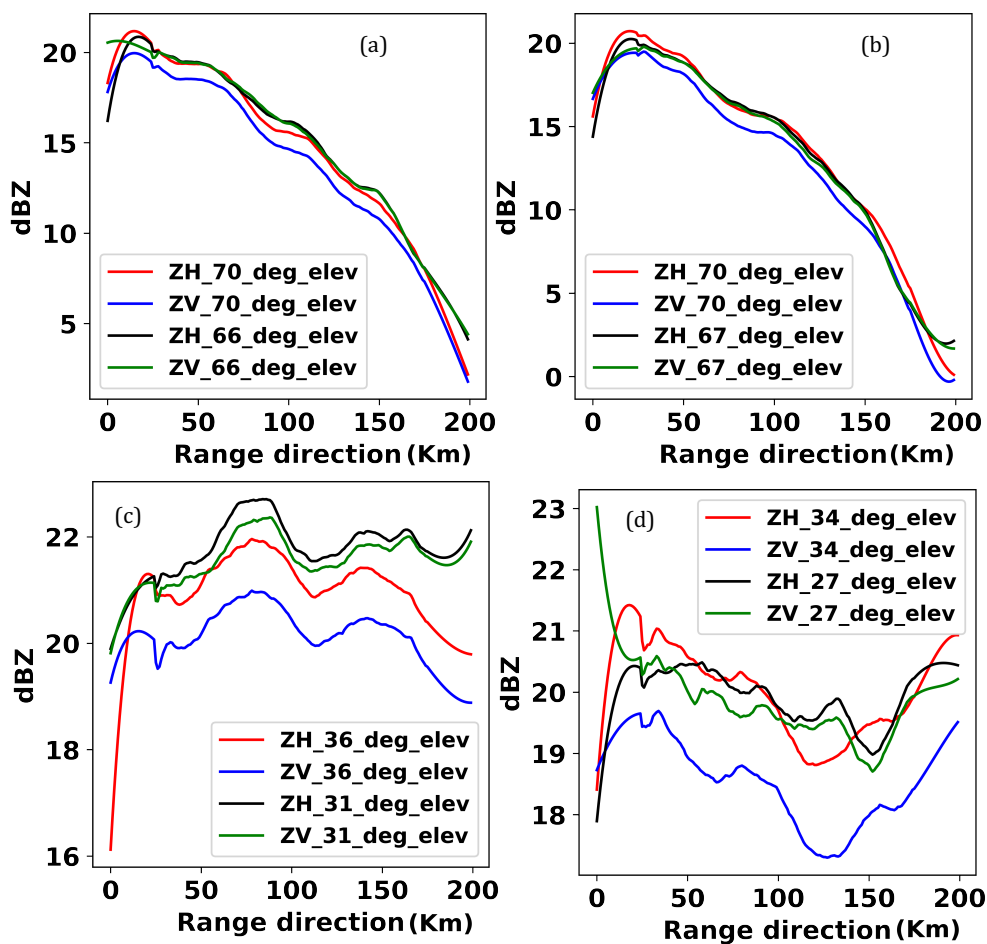
214

215



216  
217  
218  
219

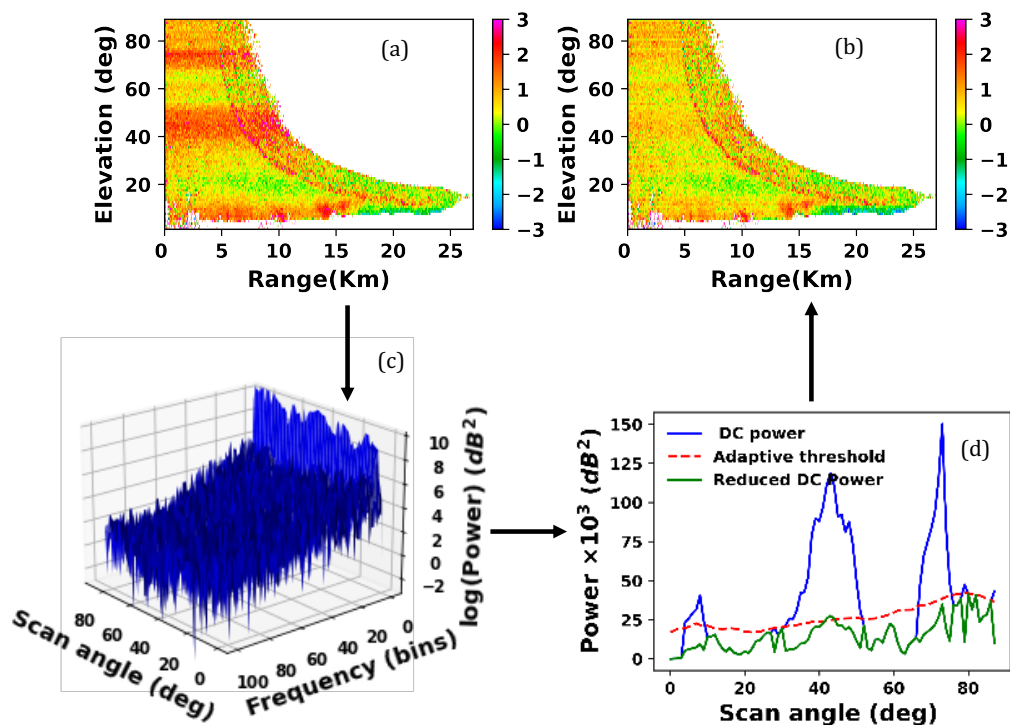
**Fig. 1.** Photographs illustrating the structure and assembly of the four lateral panels of the ESPOIRS Radar radome showing the regions of metal nuts and bolts (a), (b), (c). Distribution of PHIDP offset obtained from all the PPI scans observed on 3<sup>rd</sup> February 2022 (d).



220  
221  
222  
223  
224  
225  
226

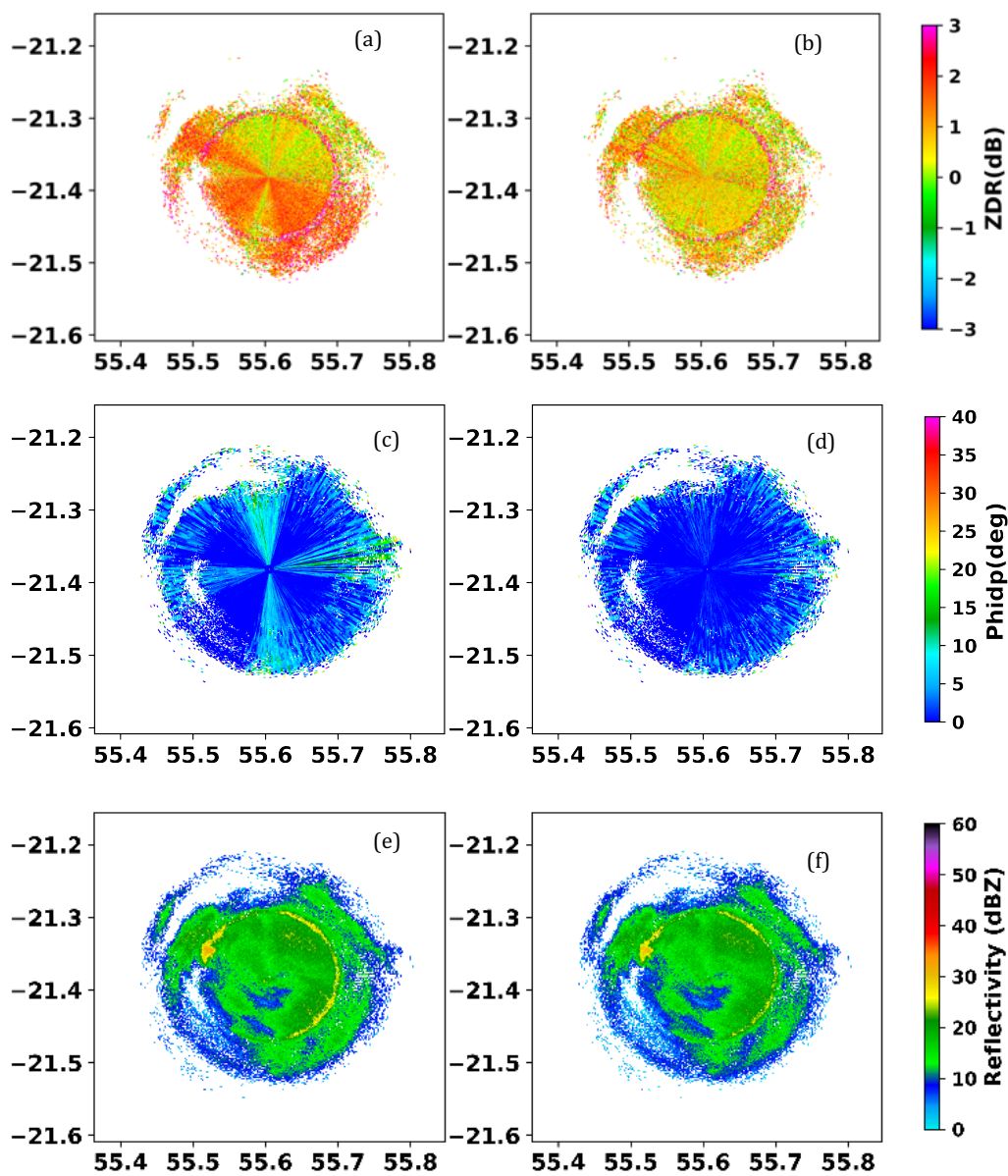
**Fig. 2.** The temporal median of horizontal and vertical reflectivity was obtained from RHI scan angles of (a) 28°, (b) 300°, (c) 45°, and (d) 76°, with corresponding elevation angles showing positive ZDR bias in red and blue (70°, 36°, and 34°) and unbiased elevation angles in green and black (66°, 67°, 31°, and 27°) on February 3rd, 2022.





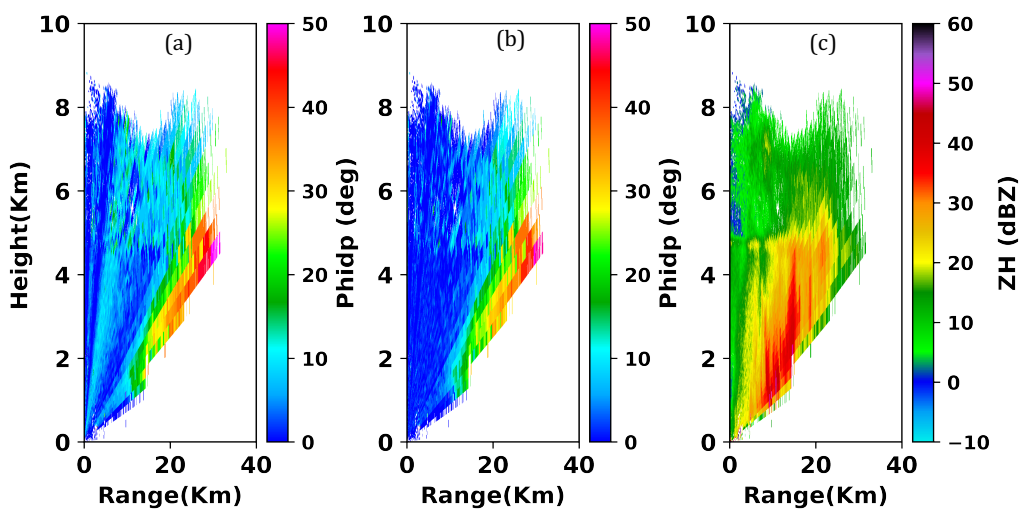
227  
228  
229  
230  
231

**Fig. 3.** 76° RHI scan of ZDR measured on 3<sup>rd</sup> February 2022 01:08 UTC before and after correction (a,b), 3D power spectrogram (c), The power from zeroth frequency (DC) component (blue), adaptive threshold values (dotted red) and the reduced zeroth frequency power after the application of the correction factor (d).



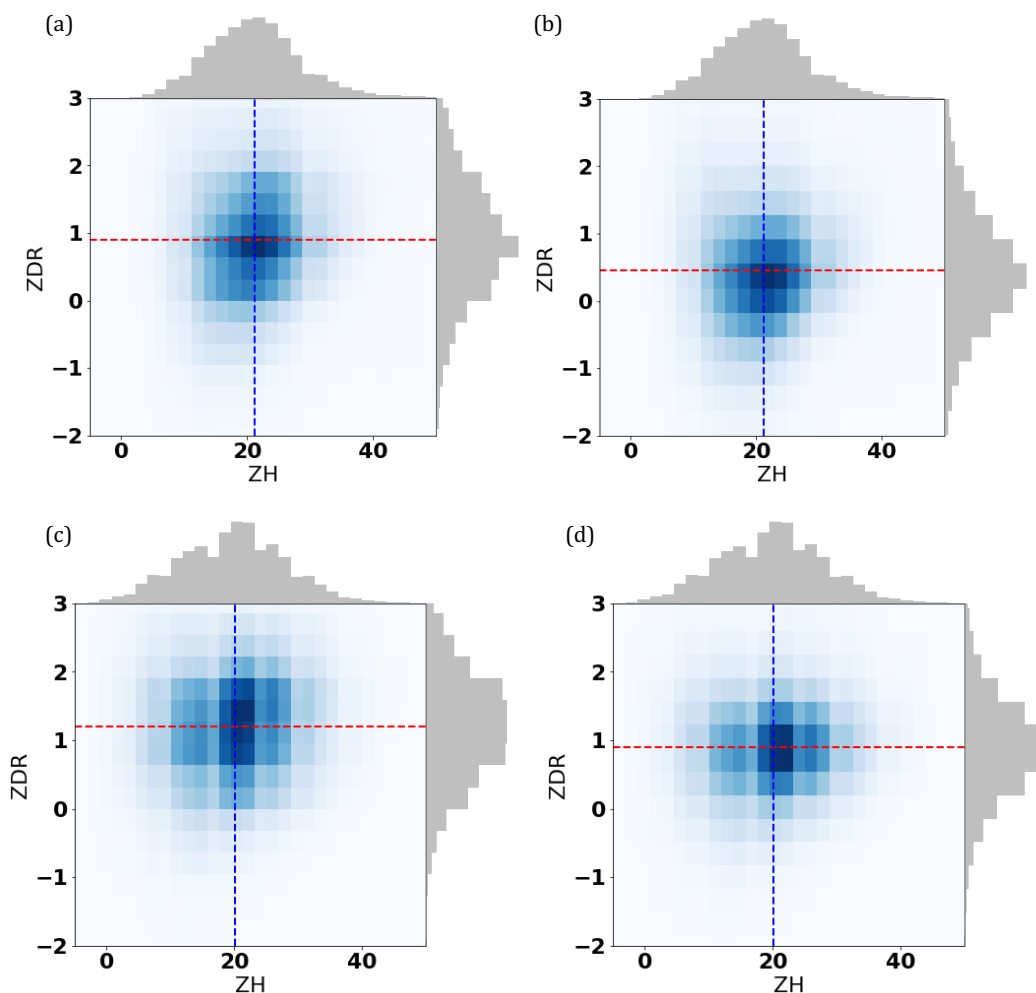
232  
233  
234  
235  
236

Fig. 4. 29° PPI scan of ZDR, PHIDP before correction (a, c) and after correction (b, d), horizontal (e) and vertical reflectivity (f) measured on 03 February 2022 01:50 UTC.



237  
238  
239

Fig. 5. 28° RHI scan of PHIDP before and after correction (a, b) along with ZH (c) on 03 February 2022 01:28 UTC.



240



241 **Fig. 6.** Joint histograms of ZDR and ZH for (a) PPI scans before and (b) after correction, as well as (c) RHI scans before and (d) after  
242 correction, all from scans conducted on February 3, 2002, with the marginal distribution of ZH in the top and the marginal distribution of ZDR  
243 on the right side. The red dotted line represents the median of ZDR, while the blue dotted line represents the median of ZH.  
244  
245

## 246 References

- 247  
248 Figueras i Ventura, J., Boumahmoud, A. A., Fradon, B., Dupuy, P., and Tabary, P.: Long-term monitoring of French  
249 polarimetric radar data quality and evaluation of several polarimetric quantitative precipitation estimators in ideal conditions for  
250 operational implementation at C-band, *Quarterly Journal of the Royal Meteorological Society*, 138,  
251 <https://doi.org/10.1002/qj.1934>, 2012.  
252 Figueras i Ventura, J., Schauwecker, Z., Lainer, M., and Grazioli, J.: On the Effect of Radome Characteristics on Polarimetric  
253 Moments and Sun Measurements of a Weather Radar, *IEEE Geoscience and Remote Sensing Letters*, 18, 642–646,  
254 <https://doi.org/10.1109/LGRS.2020.2981993>, 2021.  
255 Frech, M., Lange, B., Mammen, T., Seltmann, J., Morehead, C., and Rowan, J.: Influence of a radome on antenna  
256 performance, *J Atmos Ocean Technol*, 30, <https://doi.org/10.1175/JTECH-D-12-00033.1>, 2013.  
257 Georgis, J. F., Roux, F., and Hildebrand, P. H.: Observation of Precipitating Systems over Complex Orography with  
258 Meteorological Doppler Radars: A Feasibility Study, *Meteorology and Atmospheric Physics*, 72, 185–202,  
259 <https://doi.org/10.1007/s007030050015>, 2000.  
260 Gourley, J. J., Tabary, P., and du Chatelet, J. P.: Data Quality of the Meteo-France C-Band Polarimetric Radar, *J Atmos Ocean*  
261 *Technol*, 23, 1340–1356, <https://doi.org/https://doi.org/10.1175/JTECH1912.1>, 2006.  
262 Li, P., Li, N., Xu, W., and Song, L.: Phase Compensation of Composite Material Radomes Based on the Radiation Pattern,  
263 *Chinese Journal of Mechanical Engineering (English Edition)*, 30, <https://doi.org/10.1007/s10033-017-0133-1>, 2017.  
264 Mishra, S., Sarkar, M., and Daniel, A.: Optimization of radome wall and joint for X-band reflector antenna using Floquet  
265 modal analysis, *J Electromagn Waves Appl*, 28, 1257–1268, <https://doi.org/10.1080/09205071.2014.914859>, 2014.  
266 Park, S.-G., Bringi, V. N., Chandrasekar, V., Maki, M., and Iwanami, K.: Correction of Radar Reflectivity and Differential  
267 Reflectivity for Rain Attenuation at X Band. Part I: Theoretical and Empirical Basis, *J Atmos Ocean Technol*, 22, 1621–1632,  
268 <https://doi.org/https://doi.org/10.1175/JTECH1803.1>, 2005.  
269 Ryzhkov, A. V., Zhuravlyov, V. B., and Rybakova, N. A.: Preliminary Results of X-Band Polarization Radar Studies of  
270 Clouds and Precipitation, *J Atmos Ocean Technol*, 11, 132–139, [https://doi.org/https://doi.org/10.1175/1520-0426\(1994\)011<0132:PROXBP>2.0.CO;2](https://doi.org/https://doi.org/10.1175/1520-0426(1994)011<0132:PROXBP>2.0.CO;2), 1994.  
271  
272  
273